SCIENTIFIC REPORTS

OPEN

SUBJECT AREAS:
POLLUTION REMEDIATION
PHOTOCATALYSIS

Received
24 June 2014

Accepted
22 August 2014

Published
11 September 2014

Correspondence and requests for materials should be addressed to J.Z. (jlzhang@ecust.edu.cn)

Highly-dispersed Boron-doped Graphene Nanosheets Loaded with TiO_2 Nanoparticles for Enhancing CO_2 Photoreduction

Mingyang Xing, Fan Shen, Bocheng Qiu & Jinlong Zhang

Key Laboratory for Advanced Materials and Institute of Fine Chemicals, East China University of Science and Technology, 130 Meilong Road, Shanghai 200237, P.R. China.

Boron doped graphene nanosheets (B-GR) as a p-type semiconductor, provides much more edges to facilitate the loading of TiO_2 nanoparticles (P25). Highly-dispersed P25/B-GR nanosheets with the size of 20-50 nm, are successfully synthesized by the vacuum activation and ultraphonic method. The nanosized morphology can decrease the local density of defects which are induced by the boron substitutional doping, and make the B-GR keeping excellent conductivity and p-type transport property. Ti-O-C bonds are formed during the mixing process, which could efficiently transfer the electrons from TiO_2 to B-GR and the holes from B-GR to TiO_2. The tunable bandgap of B-GR determines the large potential application of P25/B-GR in the photoreduction of CO_2 and other gaseous organic pollutants.

As one of the gases to cause the global-warming effects, CO_2 is very stable and inertia, which makes it difficult to be activated, thus, a harsh reaction condition and a high energy consumption are needed to achieve its conversion to the clean fuels and value-added chemicals. Since the successful works in 1979 by Fujishima et al.[1] to report the photoelectrocatalytic reduction of CO_2 to form organic compounds such as formic acid, formaldeyde, methyl alcohol and methane, in the presence of photosensitive semiconductor powders suspended in water as catalysts, many studies have been focused on the modification of TiO_2 in order to exploit its application to the CO_2 photoreduction[2–7]. As an ideal photocatalyst, nanoscaled TiO_2 was widely used in the photodegradation of organic pollutants[8,9], due to its inexpensive, non-toxic, high stability, and other advantages[10–13]. However, there are some major obstacles that hinder its industrialization, such as: (1) pure TiO_2 can only absorb the ultraviolet light, which is inefficient use of solar energy; (2) it has a high recombination rate between photo-excited holes and electrons, and a low quantum efficiency[14]. The composite comprised of TiO_2 and carbon materials is expected to break the above mentioned application bottlenecks of TiO_2[13,15], which is considered to be one of the most development potential of photocatalytic material types.

Compared with some other carbon materials such as nanotubes and fullerenes, graphene (GR) has excellent conductive property, mechanical property and chemical stability[16,17]. Its special monoatomic layers of two-dimensional structure and high surface area, allow it to become a much more ideal multifunctional material with excellent performance of carrying and passing electrons and holes, compared with other carbon materials[18,19]. However, the investigation towards the effect of graphene size on supramolecular response has remained challenging, because of the predominantly micrometer-sized and polydisperse nature of chemically exfoliated graphene oxide (GO)[20,21], and there is less report on successful preparation of dispersed graphene nanosheets, whose size are controlled within 20 ~ 50 nm, up to now. In order to further improve the electronic properties of graphene, many researches have been focus on doping graphene with impurity atoms, such as boron and nitrogen[22–27]. For instance, boron doping in GR sheets could achieve the tuning of bandgaps and cause the B-GR sheets showing p-type transport properties[25]. However, the boron doping also could introduce a large number of defects in the skeleton of large-scaled GR sheets, which indeed reduced the electronic transmission of GR. Hence, controlling the graphene size in nanoscale is considered as a useful method to decrease the topical defects density in GR sheets. The decrease size of GR can not only efficiently reduce the local density of defects but also increase the exposure of ZZ-edges to improve the semimetallic property of B-GR, which induces enhanced electrical conductibility[28–30].

On the other hand, despite various reports on composites of TiO_2-graphene[15,31,32], however, in those research works, some significant and key issues remain unaddressed completely[32], and some questions are naturally raised. How do the TiO_2 and graphene connect together? What induces the visible light absorption range of composite, sensitization of graphene or introduction of impurity level inside TiO_2? What is the effect of impurity elements doping on the electrons transfer capacity of graphene? Besides the unresolved above mentioned questions, there is hitherto less reports on application of TiO_2-graphene composite to the photoreduction of CO_2.

Herein, we employed a simple vacuum reduction and ultraphonic method to prepare a graphene and a boron doped graphene with nanoribbons structure according to our previous report[28], by using GO as the precursor and boric acid as the boron source, which were denoted as GR and B-GR, respectively. The boron doped graphene nanoribbons give the semimetallic properties with low impedance owing to the exposure of ZZ-edges[28–30]. The B-GR loaded with TiO_2 nanocomposite was synthesized through an ultraphonic mixing method, using the commercial TiO_2 nanoparticles of P25 as the raw material, which was denoted as P25/B-GR. After loading with P25, the B-GR nanoribbons were fully cut into highly-dispersed nanosheets, and the increase expose of edges determines the semimetallic property of B-GR. The GO and GR loaded with TiO_2 nanocomposites were prepared by using the micrometer-sized GO sheets as the precursor, through a similar method and denoted as P25/GO and P25/GR, respectively. Compared with the conventional micrometer-sized GR, nanometer-sized B-GR could greatly enhance the electron locality and achieve the directional transfer of photoproduced electrons on the graphene, as well as the contact chance between the graphene and the target molecules, hence improving the photocatalytic efficiency of the P25/B-GR.

Results

Figure 1 shows the TEM images of GR, B-GR and P25/B-GR. Our previous work has found that the GO presents a polydispersed micrometer-sized structure and exhibits some wrinkles[28]. After vacuumed reduction and ultraphonic treatment, the GR maintains the decreased micrometer-sized structure, while after boron doping, the large scaled graphene sheets are cut into nanoribbons (Figure 1a, b)[28]. Our previous work has reported that the macro-residual stress induced by the boron substitutional doping is responsible for the formation of nanoribbons[28], which is very similar to the cutting of carbon nanotubes into graphene nanoribbons by the reoxidation and hydrothermal method[33,34]. It is noteworthy some ZZ-edges and AC-edges are exposing with the cutting of graphene sheets (Figure 1b)[28]. The doping of boron successfully achieve the decrease of the size of GR sheets and the improvement of the conductivity of B-GR (Figure S1, the impedance comparison among GO, GR and B-GR)[28]. Interestingly, when the P25 nanoparticles are mixed with B-GR and followed by an ultraphonic treatment, the nanoribbons structure is further cut into the smaller nanosheets, as shown in Figure 1c. Although the B-GR nanoribbons were cut into smaller nanosheets after loading with TiO_2 nanoparticles, they still maintain the ZZ-edges as well as the semimetallic properties. The TiO_2 nanoparticles are highly-dispersed loading on B-GR nanosheets surface, rather than aggregated on micrometer-sized graphene surface reported by others[15,31,32,35]. The TiO_2 particle size is about 10–20 nm and the size of B-GR nanosheet is approximately 20–50 nm, seen from the HRTEM image in Figure 1d. The interdistance of lattice plane of 0.351 nm is indexed to the (101) plan of TiO_2, and the adjacent nanosheets is the B-GR. The XRD spectra for different P25-graphene composites indicate that the ultraphonic mixing cannot change the crystal form of P25 (Figure 2), and all the TiO_2 exhibit anatase and rutile mixed crystal and the crystal size also remains constant in the range of 10–20 nm, which is accordance with the HRTEM results.

In order to study the formation of B-GR nanosheets after loading with TiO_2, the interaction between TiO_2 and B-GR are investigated by the analysis of XPS results of graphene and P25/B-GR, as shown in Figure 3[28]. Our previous work on boron doped graphene nanoribbons has demonstrated the formation of B_4C and BC_3 structures in B-GR, which indicates the substitutional doping of boron into the skeleton of graphene[28]. The C1s XPS spectra of different samples are given to prove the existence of Ti-O-C (Figure 3a). The decrease of the peaks at 285.7 and 286.8 eV indicates the successful reduction of GO in the process of vacuum activation. Compared with the GR, after the addition of H_3BO_3, the characteristic peaks of C-OH and C-O-C on B-GR have an obviously decrease, indicating that the substitutional doping of boron could improve the reduction of GR

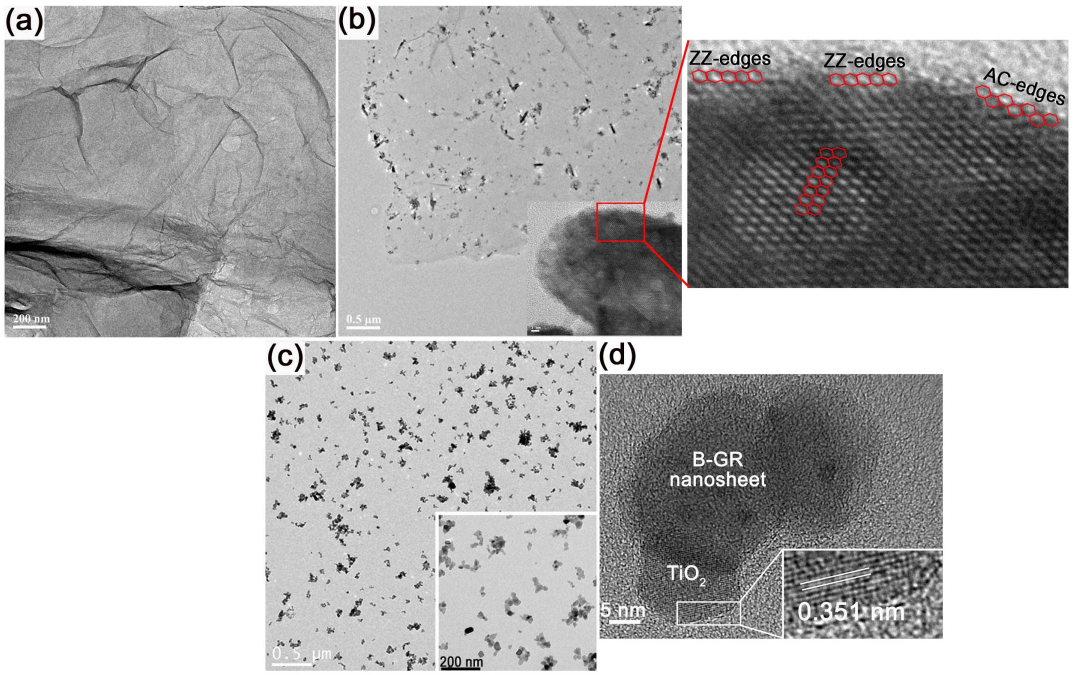

Figure 1 | TEM images of samples. Low magnification TEM and high-resolution TEM (HRTEM) images of GR (a), B-GR (b)[28], and P25/B-GR (c, d).

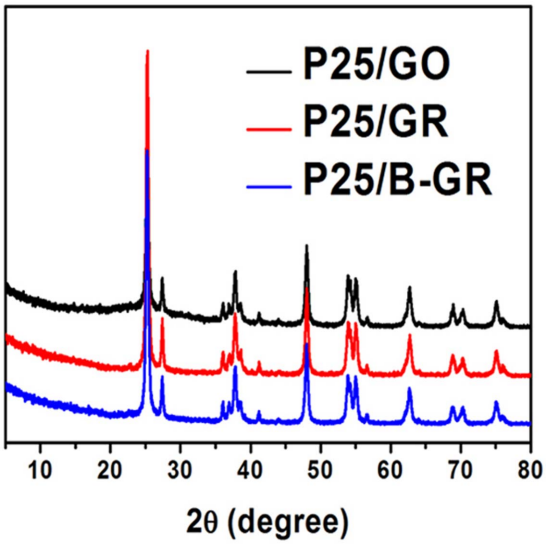

Figure 2 | **XRD spectra for different samples.**

(Figure 3a). Hence, it is expected to have a high conductivity for the B-GR. And a new peak of C-B generated at 285.3 eV in Figure 3a, suggests the interaction between boron and graphene[28]. After loading with TiO_2 nanoparticles, there is appearing a new peak at approximately 285.5 eV with a strong intensity, owing to the formation of Ti-O-C bonds. And another new peak at 289.4 eV can be ascribed to the Ti-O-C=O structure. During the stirring and ultraphonic process, the OH- groups on P25 are reacted with the residual OH- and OH-C=O bonds on B-GR to form the Ti-O-C and Ti-O-C=O structures. That means the occurrence of intermolecular dehydration between Ti-OH and these oxidation groups on the edge of B-GR to form the Ti-O-C structures. The Ti2p XPS spectra presented in Figure 3b also demonstrate the generation of Ti-O-C structures. The $Ti2p_{3/2}$ shifts from 458.2 to 458.8 eV after loading with B-GR, indicating that some Ti-O-Ti bonds were replaced by Ti-O-C due to higher electronegativity of C than Ti. In addition to generate the Ti-O-C on P25/B-GR, the loading of TiO_2 nanoparticles on the surface of B-GR also has a possibility to produce the Ti-O-B bonds, which also can cause a similar red-shift of $Ti2p_{3/2}$ peaks in Figure 3b. Thereby, in order to eliminate the formation of Ti-O-B, the O1s XPS spectra for P25/GR and P25/B-GR are given in Figure 3c. There is an obvious characteristic peak of Ti-O-C at 531.2 eV in the O1s XPS spectra of P25/GR and P25/B-GR, and the absence of the peak at 532.7 eV indicates the absence of Ti-O-B in P25/B-GR[36]. All the above mentioned XPS results confirm that the simple stirring-ultraphonic treatment can produce some Ti-O-C bonds to strengthen the interaction between TiO_2 and graphene. Different from

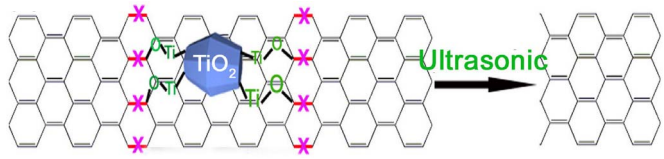

Figure 4 | **Schematic diagram of the cutting of B-GR nanoribbons into nanosheets in the presence of TiO_2 nanoparticles.**

other TiO_2-graphene composites prepared by the chemical synthesis methods[15,31,37,38], we use a simple stirring-ultraphonic method to successfully load the TiO_2 nanoparticles on graphene surface by the connection bonds of Ti-O-C rather than Ti-C generated in other reports[31,39–42]. Zhang et al.[43] found that the P25/GO composite prepared by a stirring mixed method showed an enhanced photocatalytic activity under the solar light irradiation, which implied the interaction between GR and TiO_2 during the stirring-ultraphonic process. The chemical bonds between P25 and B-GR play an important role in the cutting of nanoribbons into nanosheets, which introduce a macro-residual stress on the surface of B-GR nanoribbons and cut it into smaller pieces. It is well known that the macro-residual stress induced by the foreign impurity can cause the anisotropic lattice contraction[28]. The loading of TiO_2 on GR surface exhibits a distinct pressure stress, which causes the rupture of C-C bonds close to Ti-O-C in B-GR nanoribbons, by a shear force from the ultraphonic treatment (Figure 4). Our previous work has found that the ultraphonic energy can cut some large-scaled GR into smaller sheets only when the ultraphonic time is prolonged to 6 h (Figure S2a)[28]. When the ultraphonic time is limited in 1 h, there is only less nanosheets presence in B-GR (Figure S2b). However, in the presence of TiO_2 nanoparticles, the B-GR can be completely cut into highly-dispersed nanosheets after ultraphonic for 1 h (Figure 1c). That means the macro-residual stress induced by the loading of TiO_2 is the major reason for the formation of nanosheets.

In addition to the loading of TiO_2, there is also another important factor to determine the formation of highly-dispersed nanosheets, that is, the doping of boron in GR. The TEM images of P25 mixed with GR (P25/GR) are shown in Figure 5. Although the macro-residual stress induced by the loading of TiO_2 can cut the large-scaled GR sheets into much smaller sheets, there are also some large-scaled sheets found in Figure 5, and the dispersion of P25/GR nanosheets is much poorer compared with that of the P25/B-GR (Figure 1c). An obvious aggregation can be found in the TEM image of P25/GR (Figure 5). It is because that the boron doping has cut the large-scaled GR sheets into some nanoribbons (Figure 1b), and the further loading of TiO_2 nanoparticles facilitates the cutting of nanoribbons into smaller nanosheets (Figure 1c, d), which induces the formation of the highly-dispersed and lowly-aggregated B-GR nanosheets. The

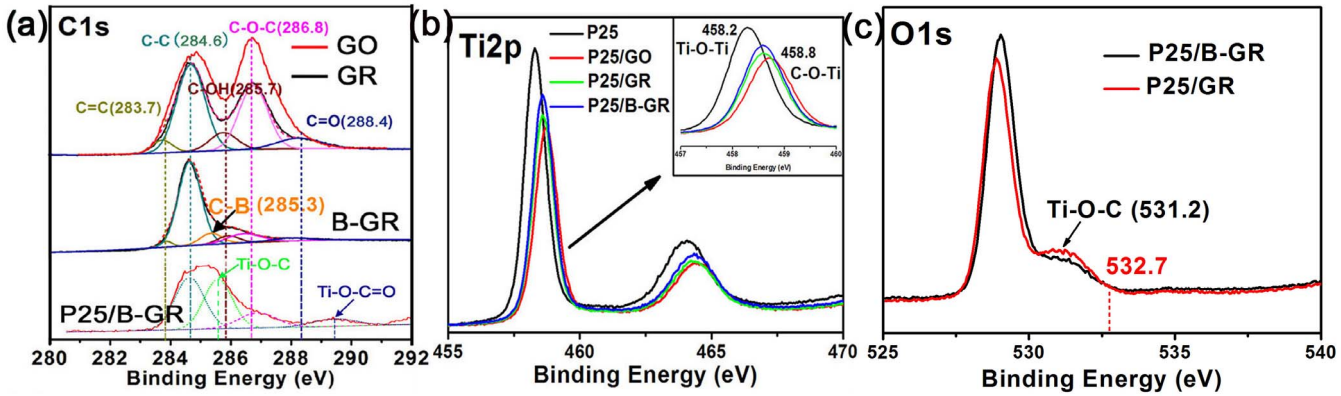

Figure 3 | **XPS analysis.** C1s (a), Ti2p (b) and O1s (c) XPS spectra for different samples.

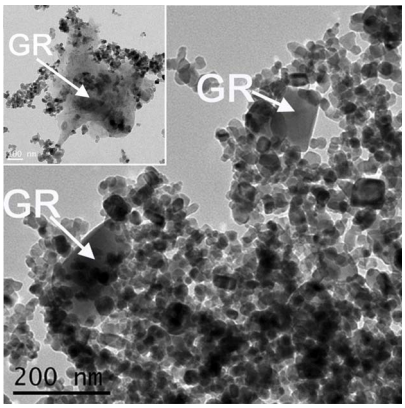

Figure 5 | TEM images for P25/GR.

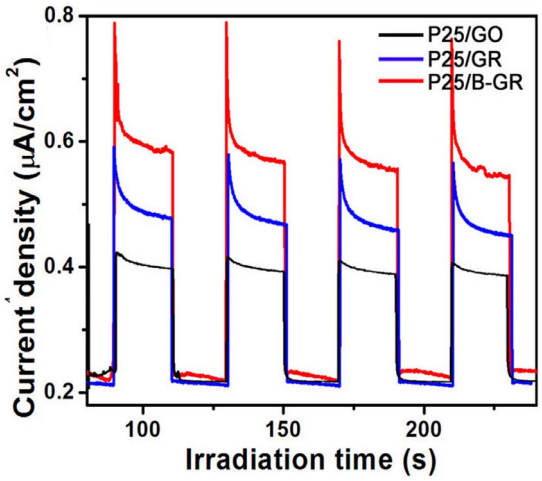

Figure 6 | Photocurrent spectrum measurement. Transient photocurrent responses of P25/GO, P25/GR and P25/B-GR in 0.5 M Na_2SO_4 aqueous solution under solar irradiation.

studied GR without boron doping is prepared by using the micrometer-sized GO sheets as the precursor. After loading with P25, although the size of GR in Figure 5 has a certain degree of reduced, it is still too large to expose enough edges and to give a semimetallic property. Instead of that, GR is more likely to be a semiconductor[44]. Compared with other reported large-scaled GR sheets/TiO_2 composites[15,31,32,35], our prepared nano-sized B-GR presents decreased topical defects density, much lower impedance, and excellent conductivity (Figure S1, impedance spectra for different samples)[28], which determine the large potential application of P25/B-GR in the photocatalysis. Additionally, the P25/B-GR can produce the electrons and exhibit a high photocurrent response under the simulated solar light irradiation, as shown in Figure 6.

The solar-driven photocatalytic activity of P25/B-GR nanocomposite was measured by monitoring the methane generation during photocatalytic reduction of CO_2, as shown in Figure 7a. After boron substitutional doping into graphene, the B-GR has a p-type semiconductor property[25], which can connect with the n-type semiconductor of TiO_2 to form the n-p junction. When a n-p junction is formed in a photocatalytic system, the photo-generated hole-electron pairs can be immediately separated under internal electrostatic field in the p-n junction region[45–47]. The electrons will move to the p-type semiconductor of B-GR and the holes will transfer to the n-type semiconductor of TiO_2 to minimize the recombination rate and increase the quantum yield[46]. However, in the photo-reduction system such as water splitting and CO_2 reduction, the addition of hole scavenger is still very important to the photo-reduction efficiency of electrons[47], owing to the presence of recombination between holes and electrons in the bulk of n-type semiconductors. Some studies have reported that the ethanol or sodium carbonate is used as the sacrificial hole scavenger in the p-n junction system for the water splitting or photoreduction of hexachloroplatanic acid[46,47]. For instance, Meng et al.[47] prepared the n-p junction of MoS_2/nitrogen doped graphene, which also needed the ethanol as the sacrificial hole scavenger in the water splitting. Hence, although the presence of B-GR is beneficial to the transfer of holes, the addition of sacrificial hole scavenger in the CO_2 photoreduction process is still necessary to further improve the photo-reduction efficiency of electrons.

In addition to CO_2, some reports have found that the graphene or other carbon species also can be photoreduced by the TiO_2 to generate carbonate products under the light irradiation[48,49]. In order to confirm the existence of CO_2 photoreduction in our investigation, the blank photocatalytic test of P25/B-GR in the absence of CO_2 is given in Figure 7a. Obviously, there is only a little CH_4 (< 0.35 μmol/g) generated after 120 min solar light irradiation. On the other hand, the P25/B-GR shows the highest photogenration of CH_4 ($>$ 2.50 μmol/g), which is much higher than that of the P25/B-GR in the absence of CO_2. Thereby, we can conclude that the generated CH_4 has its origin on the photoreduction of CO_2 rather than the photodegradation of graphene. In all the composites, the P25/B-GR shows the highest photoreduction efficiency of CO_2. The photoreduction of CO_2 includes two basic procedures: first is the CO_2 molecules adsorbed on the reaction sites of photocatalyst; second is the reaction conversion between CO_2 and photo-excited electrons and holes. Hence, the interaction between graphene and TiO_2 plays an important role in the transfer of electrons. In addition, although all the TiO_2/graphene composites exhibit a little enhancing adsorption capacities of methyl orange (MO) compared with the pure P25 (Figure S3), the P25/B-GR has substantial activity in the photocatalytic degradation of MO under visible light irradiation, as shown in Figure 7b. Under the solar light irradiation, the photo-excited electrons on CB of TiO_2 are injecting into the B-GR, and the photo-excited holes located on B-GR transfer into the VB of TiO_2 through the Ti-O-C bonds, owing to the p-type property of B-GR[25,50], as shown in Figure 8a. Finally, the electrons are concentrating upon the B-GR nanosheets, and the holes are concentrating upon the TiO_2 nanoparticles, which are authentically realizing the separation of photoproduced electrons and holes.

Discussion

It is a remarkable fact that, compared with micrometer-sized graphene loaded with TiO_2 (P25/GR), the nanometer-sized structure of graphene could effectively reduce the transmission distance and induce the occurrence of scattering by the further boron doping. In fact, the electronic property of graphene oxide is similar with that of graphite oxide[28], and both of them are semiconductors[51,52]. And the GR can also be considered as a reduced GO, due to its incomplete reduction in the vacuum at a relative low temperature. That is to say the GR is also a semiconductor. However, further doping with boron, the graphene exhibits a semimetallic property. Some studies on GR have reported that the edges in GR sheets and few-layer graphene nanoribbons have highly reactive sites, which can exhibit metallic and semiconductor properties simultaneously[28,44]. The exposure of ZZ-edges on nanoscaled graphene is easier to give a semimetallic property[29,30]. In our investigation, the P25/B-GR nanosheets are prepared by using boron doped graphene nanoribbons as the precursor which has demonstrated to expose many ZZ-edges in our previous work[28]. Thereby, the photo-produced electrons of B-GR make its Fermi level ($E'_{\text{f-B-GR nanosheets}}$) being higher than the conduction band ($E_{\text{C-GR sheets}}$) of GR sheets (from $E_{\text{f-B-GR nanosheets}}$ to $E'_{\text{f-B-GR nanosheets}}$ in Figure 8b). The level of $E'_{\text{f-B-GR nanosheets}}$ just falls in between the conduction band (CB) of TiO_2 and the relevant redox potentials of CO_2/CH_4[5], which is beneficial to the transfer of photo-

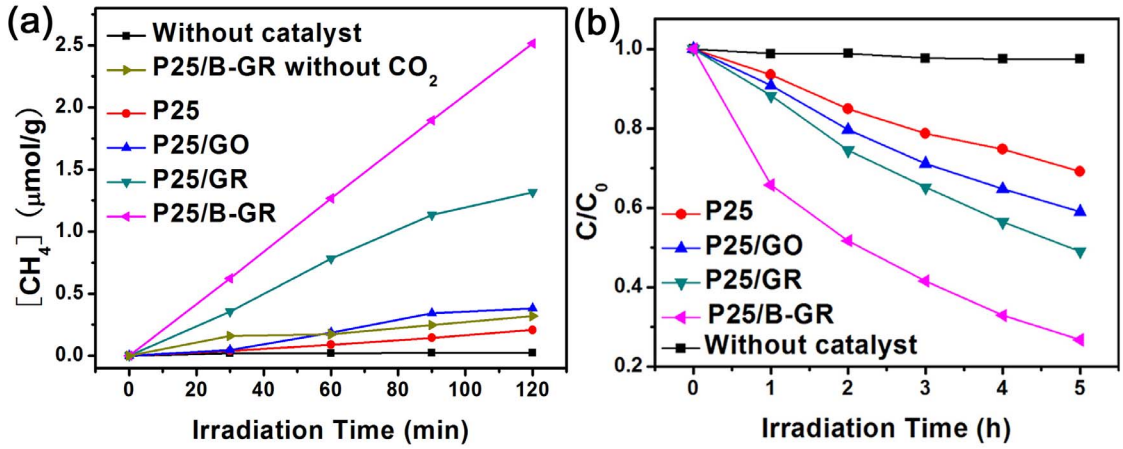

Figure 7 | Photocatalytic activities of different samples. Simulated solar light induced CO_2 reduction (The dark yellow line is the data of the blank photocatalytic test of P25/B-GR in the absence of CO_2) (a), and visible light induced photocatalytic activities for degradation of MO (b).

generated electrons, as shown in Figure 8a. Different from B-GR, the GR sheets have a relative lower CB under the level of redox potentials of CO_2/CH_4. The low reductive capacity of GR sheets determines the lower CO_2 conversion efficiency of P25/GR than that of P25/B-GR. The excellent electron-accepting and transporting capacities of B-GR could improve the electrons transfer efficiency and the reaction sites on its surface, resulting in the acceleration of the reaction conversion between CO_2 and photo-excited electrons, as summarized in reaction (1). Simultaneously, in the photo-degradation of MO, the absence of sacrificial hole scavenger promotes the collective holes on TiO_2 VB reacting with H_2O molecules to generate many mobile free OH radicals (Figure 8a). A large number of generated mobile free OH radicals are responsible for the high photocatalytic activity of P25/B-GR for the degradation of MO under the visible light irradiation.

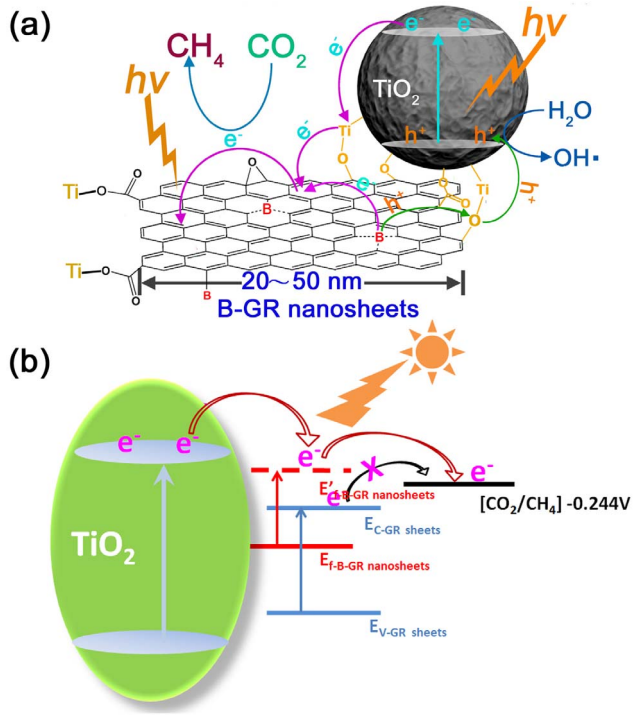

Figure 8 | Structural model of energy states. Schematic diagram of photo-excited electrons and holes transfer among TiO_2 nanoparticles and B-GR nanosheets (a). Schematic diagram of photo-generated electrons transfer between TiO_2 and graphene materials (b).

$$CO_2 + 8H^+ + 8e^- \rightarrow CH_4 + 2H_2O \quad (1)$$

In conclusion, smaller sized B-GR nanosheets were successfully prepared for the first time, through a simple vacuum reduction followed by an ultraphonic method. TiO_2 nanoparticles were loaded on the surface of B-GR nanosheets by a simple ultraphonic-stirring mixing method, which exhibit a high efficiency of CO_2 photoreduction and photodegradation for MO. The macro-residual stress induced by the formation of Ti-O-C bonds between TiO_2 and graphene is responsible for the cutting of B-GR sheets into smaller size of nanosheets. The excellent electron transporting capacities of B-GR were beneficial to the separation of photoproduced electrons and holes, resulting in the enhancement of CO_2 reduction and the generation of free OH radicals. Our results open the way to further implementation of graphene-based materials as photocatalysts that can be used in the photoreduction of CO_2 and photodegradation of other organic pollutants in the gas phase. In addition, it would be nice to explore the boron-concentration dependence photocatalytic activity of B-GR/TiO_2 hybrid materials in the future research work.

Methods

Preparation of GO, GR and B-GR. Graphite oxide (GO) was synthesized from natural graphite powder using a modified Hummers methods[53]. The detail experimental procedures were referring to the report published by Zhangpeng Li et al.[17] The preparation of B-GR is according to our previous work[28]. 5 ml GO was dispersed into 20 mL double distilled water and ultraphonic for 1 hour, and then 0.4 g H_3BO_3 was added to the above solution and vigorous stirring for 1 hour. The solution was drying at 60°C for 12 h. Obtained brown flaky solid was heated at 300°C for 3 hours in the vacuum condition. The color of flaky solid was changed from brown to black. This black solid was dispersed into 20 mL double distilled water again and ultraphonic for 1 hours. 30 ml HCl (1 M) was added to the above mentioned solution and stirring for 15 hours to washing out the boron oxides coverage on the surface of graphene. After HCl washing, the solid products were washed by the double distilled water for 5 times and dispersed into 5 mL double distilled water. Finally, it was transferred to a plastic bottle and denoted as B-GR. The GR was prepared by the above similar method without the adding of H_3BO_3.

Synthesis of TiO_2-graphene composites. 4 mL B-GR was added into 40 mL double distilled water and ultraphonic for 1 hour, and then 0.5 g P25 (Degussa) was added to the solution. The mixture solution was treated with ultraphonic for 1 hour and vigorous stirring for 5 hours. The mixture was dried under 80°C and denoted as P25/B-GR. In the same way, 4.0 ml B-GR was replaced to GO and GR to obtain the P25 loaded with GO and GR composites, which were denoted as P25/GO and P25/GR, respectively.

Characterization. X-ray diffraction (XRD) patterns of all samples were collected in the range 10–80° (2θ) using a Rigaku D/MAX 2550 diffractometer (Cu K radiation, λ = 1.5406 Å), operated at 40 kV and 100 mA. The morphologies were characterized by transmission electron microscopy (TEM, JEM2000EX). The instrument employed for X-ray photoelectron spectroscopy (XPS) studies was a Perkin-Elmer PHI 5000C

ESCA system with Al Kα radiation operated at 250 W. The shift of the binding energy due to relative surface charging was corrected using the C1s level at 284.6 eV as an internal standard. All the electrochemical experiments included electro-chemical impedance spectroscopy and photocurrents measurements were carried out on an electrochemical analyzer (CHI 660 D electrochemical station, CHI Instruments Inc.) at room temperature. A standard three-electrode system consisting of a working electrode (as-prepared samples as the working electrodes with an active area of ca. 0.5 cm^{-2}), a Pt wire as the counter electrode and a saturated Ag/AgCl as the reference electrode was employed.

Photocatalytic Activities. CO_2 photoreduction reaction was carried out in a home-made photocatalytic reactor. 0.1 g catalyst was added in 5 mL CO_2 saturated double distilled water. 0.1 g $NaSO_3$ was added in the solution as a hole scavenger. A 300 W Xe lamp (Newport) was used as a light source to simulate the solar light. At the given time intervals, the produced CH_4 were taken from the mixture and immediately measured by gas chromatography (Techcomp GC-7890II) with a flame ionization detector (FID).

Visible light-driven photocatalytic activity of each sample was evaluated in terms of the degradation of methyl orange (MO, 10 mg/L). The photocatalyst (0.07 g) was added into a 100 mL quartz photoreactor containing 70 mL of an organic pollution solution. The mixture was stirred for 120 min in the dark in order to reach the adsorption–desorption equilibrium. A 500-W tungsten halogen lamp equipped with a UV cut-off filters ($\lambda > 420$ nm) was used as a visible light source. At the given time intervals, the analytical samples were taken from the mixture and immediately centrifuged, then filtered through a 0.22 μm Millipore filter to remove the photocatalysts. The filtrates were analyzed by recording variations in the absorption in UV-vis spectra of MO using a Cary 100 ultraviolet visible spectrometer.

1. Inoue, T., Fujishima, A., Konishi, S. & Honda, K. Photoelectrocatalytic reduction of carbon dioxide in aqueous suspensions of semiconductor powders. *Nature* **277**, 637–638 (1979).
2. Anpo, M. & Chiba, K. Photocatalytic reduction of CO_2 on anchored titanium oxide catalysts. *J. Mol. Catal.* **74**, 207–212 (1992).
3. Yamashita, H. *et al.* Reduction of CO_2 with H_2O on TiO_2 (100) and TiO_2 (110) Single Crystals under UV-irradiation. *Chem. Lett.* **23**, 855–858 (1994).
4. Slamet, Nasution, H. W., Purnama, E., Kosela, S. & Gunlazuardi, J. Photocatalytic reduction of CO_2 on copper-doped Titania catalysts prepared by improved-impregnation method. *Catal. Commun.* **6**, 313–319 (2005).
5. Wang, C., Thompson, R. L., Baltrus, J. & Matranga, C. Visible light photoreduction of CO_2 using CdSe/Pt/TiO_2 heterostructured catalysts. *J. Phys. Chem. Lett.* **1**, 48–53 (2009).
6. Fu, Y. *et al.* An amine-functionalized titanium metal–organic framework photocatalyst with visible-light-induced activity for CO_2 reduction. *Angew. Chem., Int. Ed.* **51**, 3364–3367 (2012).
7. Wang, W.-N. *et al.* Size and structure matter: enhanced CO_2 photoreduction efficiency by size-resolved ultrafine Pt nanoparticles on TiO_2 single crystals. *J. Am. Chem. Soc.* **134**, 11276–11281 (2012).
8. Luttrell, T. *et al.* Why is anatase a better photocatalyst than rutile? - Model studies on epitaxial TiO_2 films. *Sci. Rep.* **4**, 4043; DOI:10.1038/srep04043 (2014).
9. Cheng, C. *et al.* Enhanced photocatalytic performance of TiO_2-ZnO hybrid nanostructures. *Sci. Rep.* **4**, 4181; doi:10.1038/srep04181 (2014).
10. Xing, M., Zhang, J. & Chen, F. New approaches to prepare nitrogen-doped TiO_2 photocatalysts and study on their photocatalytic activities in visible light. *Appl. Catal., B* **89**, 563–569 (2009).
11. Feng, X., Zhu, K., Frank, A. J., Grimes, C. A. & Mallouk, T. E. Rapid charge transport in dye-sensitized solar cells made from vertically aligned single-crystal rutile TiO_2 nanowires. *Angew. Chem., Int. Ed.* **51**, 2727–2730 (2012).
12. Bian, Z., Tachikawa, T. & Majima, T. Superstructure of TiO_2 crystalline nanoparticles yields effective conduction pathways for photogenerated charges. *J. Phys. Chem. Lett.* **3**, 1422–1427 (2012).
13. Qiu, B., Xing, M. & Zhang, J. Mesoporous TiO_2 nanocrystals grown in situ on graphene aerogels for high photocatalysis and lithium-Ion batteries. *J. Am. Chem. Soc.* **136**, 5852–5855 (2014).
14. Zhang, J., Wu, Y., Xing, M., Leghari, S. A. K. & Sajjad, S. Development of modified N doped TiO_2 photocatalyst with metals, nonmetals and metal oxides. *Energy Environ. Sci.* **3**, 715–726 (2010).
15. Xiang, Q., Yu, J. & Jaroniec, M. Graphene-based semiconductor photocatalysts. *Chem. Soc. Rev.* **41**, 782–796 (2011).
16. Geim, A. K. Graphene: status and prospects. *Science* **324**, 1530–1534 (2009).
17. Li, Z. *et al.* Electrostatic layer-by-layer self-assembly multilayer films based on graphene and manganese dioxide sheets as novel electrode materials for supercapacitors. *J. Mater. Chem.* **21**, 3397–3403 (2011).
18. Li, D. & Kaner, R. B. Graphene-based materials. *Science* **320**, 1170–1171 (2008).
19. Zhang, W. *et al.* Ultrahigh-gain photodetectors based on atomically thin graphene-MoS_2 heterostructures. *Sci. Rep.* **4**, 3826; doi:10.1038/srep03826 (2014).
20. Chou, S. S. *et al.* Nanoscale graphene oxide (nGO) as artificial receptors: implications for biomolecular interactions and sensing. *J. Am. Chem. Soc.* **134**, 16725–16733 (2012).
21. Park, S. & Ruoff, R. S. Chemical methods for the production of graphenes. *Nat. Nanotechnol.* **4**, 217–224 (2009).
22. Chen, P. *et al.* Nitrogen-doped graphene/ZnSe nanocomposites: hydrothermal synthesis and their enhanced electrochemical and photocatalytic activities. *ACS Nano* **6**, 712–719 (2012).
23. Guo, B. *et al.* Controllable N-doping of graphene. *Nano Lett.* **10**, 4975–4980 (2010).
24. Sheng, Z.-H., Gao, H.-L., Bao, W.-J., Wang, F.-B. & Xia, X.-H. Synthesis of boron doped graphene for oxygen reduction reaction in fuel cells. *J. Mater. Chem.* **22**, 390–395 (2012).
25. Tang, Y.-B. *et al.* Tunable band gaps and p-type transport properties of boron-doped graphenes by controllable ion doping using reactive microwave plasma. *ACS Nano* **6**, 1970–1978 (2012).
26. Wang, X. *et al.* N-doping of graphene through electrothermal reactions with ammonia. *Science* **324**, 768–771 (2009).
27. Wang, Y., Shao, Y., Matson, D. W., Li, J. & Lin, Y. Nitrogen-doped graphene and its application in electrochemical biosensing. *ACS Nano* **4**, 1790–1798 (2010).
28. Xing, M., Fang, W., Yang, X., Tian, B. & Zhang, J. Highly-dispersed boron-doped graphene nanoribbons with enhancing conductibilities and photocatalysis. *Chem. Commun.* **136**, 5852–5855 (2014).
29. Li, Z., Yang, J. & Hou, J. G. Half-metallicity in edge-modified zigzag graphene nanoribbons. *J. Am. Chem. Soc.* **130**, 4224–4225 (2008).
30. Biel, B., Triozon, F., Blase, X. & Roche, S. Chemically induced mobility gaps in graphene nanoribbons: a route for upscaling device performances. *Nano Lett.* **9**, 2725–2729 (2009).
31. Zhang, H., Lv, X., Li, Y., Wang, Y. & Li, J. P25-graphene composite as a high performance photocatalyst. *ACS Nano* **4**, 380–386 (2009).
32. Zhang, Y., Tang, Z.-R., Fu, X. & Xu, Y.-J. TiO_2-graphene nanocomposites for gas-phase photocatalytic degradation of volatile aromatic pollutant: is TiO_2-graphene truly different from other TiO_2-carbon composite materials? *ACS Nano* **4**, 7303–7314 (2010).
33. Kosynkin, D. V. *et al.* Longitudinal unzipping of carbon nanotubes to form graphene nanoribbons. *Nature* **458**, 872–876 (2009).
34. Pan, D., Zhang, J., Li, Z. & Wu, M. Hydrothermal route for cutting graphene sheets into blue-luminescent graphene quantum dots. *Adv. Mater.* **22**, 734–738 (2010).
35. Xiang, Q., Yu, J. & Jaroniec, M. Synergetic effect of MoS_2 and graphene as cocatalysts for enhanced photocatalytic H_2 production activity of TiO_2 nanoparticles. *J. Am. Chem. Soc.* **134**, 6575–6578 (2012).
36. Zaleska, A., Grabowska, E., Sobczak, J. W., Gazda, M. & Hupka, J. Photocatalytic activity of boron-modified TiO_2 under visible light: The effect of boron content, calcination temperature and TiO_2 matrix. *Appl. Catal., B* **89**, 469–475 (2009).
37. Gopalakrishnan, K., Joshi, H. M., Kumar, P., Panchakarla, L. S. & Rao, C. N. R. Selectivity in the photocatalytic properties of the composites of TiO_2 nanoparticles with B- and N-doped graphenes. *Chem. Phys. Lett.* **511**, 304–308 (2011).
38. Li, W. *et al.* Sol–Gel design strategy for ultradispersed TiO_2 nanoparticles on graphene for high-performance lithium ion batteries. *J. Am. Chem. Soc.* **135**, 18300–18303 (2013).
39. Etacheri, V., Michlits, G., Seery, M. K., Hinder, S. J. & Pillai, S. C. A highly efficient $TiO_{2-x}C_x$ nano-heterojunction photocatalyst for visible light induced antibacterial applications. *Acs Appl. Mater. Inter.* **5**, 1663–1672 (2013).
40. Hong, J.-Y., Lee, E. & Jang, J. Electro-responsive and dielectric characteristics of graphene sheets decorated with TiO_2 nanorods. *J. Mater. Chem. A* **1**, 117–121 (2013).
41. Huang, Q. *et al.* Enhanced photocatalytic activity of chemically bonded TiO_2/graphene composites based on the effective interfacial charge transfer through the C–Ti bond. *ACS Catal.* **3**, 1477–1485 (2013).
42. Irie, H., Watanabe, K. & Hashimoto, K. Carbon-doped anatase TiO_2 powders as a visible-light sensitive photocatalyst. *Chem. Lett.* **32**, 772–773 (2003).
43. Zhang, L., Xi, Z., Xing, M. & Zhang, J. Effects of the preparation order of the ternary P25/GO/Pt hybrid photocatalysts on hydrogen production. *Int. J. Hydrogen Energy* **38**, 9169–9177 (2013).
44. Terrones, M. *et al.* Graphene and graphite nanoribbons: Morphology, properties, synthesis, defects and applications. *Nano Today* **5**, 351–372 (2010).
45. Bach, U. *et al.* Charge separation in solid-state dye-sensitized heterojunction solar cells. *J. Am. Chem. Soc.* **121**, 7445–7446 (1999).
46. Chen, Y., Crittenden, J. C., Hackney, S., Sutter, L. & Hand, D. W. Preparation of a novel TiO_2-based p−n junction nanotube photocatalyst. *Environ. Sci. Technol.* **39**, 1201–1208 (2005).
47. Meng, F., Li, J., Cushing, S. K., Zhi, M. & Wu, N. Solar hydrogen generation by nanoscale p–n junction of p-type molybdenum disulfide/n-type nitrogen-doped reduced graphene oxide. *J. Am. Chem. Soc.* **135**, 10286–10289 (2013).
48. Akhavan, O., Abdolahad, M., Esfandiar, A. & Mohatashamifar, M. Photodegradation of graphene oxide sheets by TiO_2 nanoparticles after a photocatalytic reduction. *J. Phys. Chem. C* **114**, 12955–12959 (2010).
49. Yang, C.-C., Yu, Y.-H., van der Linden, B., Wu, J. C. S. & Mul, G. Artificial photosynthesis over crystalline TiO_2-based catalysts: fact or fiction? *J. Am. Chem. Soc.* **132**, 8398–8406 (2010).
50. Zhao, L. *et al.* Local atomic and electronic structure of boron chemical doping in monolayer graphene. *Nano Lett.* **13**, 4659–4665 (2013).
51. Chen, C. *et al.* Synthesis of visible-light responsive graphene oxide/TiO_2 composites with p/n heterojunction. *ACS Nano* **4**, 6425–6432 (2010).

52. Luo, Z., Vora, P. M., Mele, E. J., Johnson, A. T. C. & Kikkawa, J. M. Photoluminescence and band gap modulation in graphene oxide. *Appl. Phys. Lett.* **94**, 111909 (2009).
53. Hummers, W. S. & Offeman, R. E. Preparation of graphitic oxide. *J. Am. Chem. Soc.* **80**, 1339–1339 (1958).

Acknowledgments

This work has been supported by National Nature Science Foundation of China (21377038, 21237003, 21173077, 21203062), National Basic Research Program of China (2013CB632403), Science and Technology Commission of Shanghai Municipality (12230705000), Sponsored by Program of Shanghai Subject Chief Scientist (12XD1402200), the Research Fund for the Doctoral Program of Higher Education (20120074130001) and the Fundamental Research Funds for the Central Universities.

Author contributions

M.X. and J.Z. conceived and designed the experiments. M.X. prepared the samples and performed characterization. M.X., F.S., B.Q., and J.Z. were mainly responsible for preparing the manuscript. All the authors discussed the results and reviewed the manuscript.

Additional information

Supplementary information accompanies this paper at http://www.nature.com/scientificreports

Competing financial interests: The authors declare no competing financial interests.

How to cite this article: Xing, M., Shen, F., Qiu, B. & Zhang, J. Highly-dispersed Boron-doped Graphene Nanosheets Loaded with TiO_2 Nanoparticles for Enhancing CO_2 Photoreduction. *Sci. Rep.* **4**, 6341; DOI:10.1038/srep06341 (2014).